Physics of Plasmas ARTICLE pubs.aip.org/aip/pop

Synergy effects between energetic ion and energetic electron on the stability of beta-induced Alfvén eigenmode

Cite as: Phys. Plasmas **33**, 022504 (2026); doi: 10.1063/5.0295801
Submitted: 11 August 2025 · Accepted: 29 January 2026 ·
Published Online: 12 February 2026

View Online Export Citation CrossMark

L. Z. Guo,[1,2] J. Bao,[1,2,a)] W. L. Zhang,[1,2,a)] and Z. Lin[3]

AFFILIATIONS

[1]Institute of Physics, Chinese Academy of Sciences, Beijing 100190, China
[2]University of Chinese Academy of Sciences, Beijing 100049, China
[3]University of California, Irvine, California 92697, USA

[a)]**Authors to whom correspondence should be addressed:** jbao@iphy.ac.cn and wzhang@iphy.ac.cn

ABSTRACT

It has been widely observed in experiments that beta-induced Alfvén eigenmodes (BAEs) can be destabilized by both energetic ions (EIs) and energetic electrons (EEs), which are termed as i-BAE and e-BAE propagating along each diamagnetic drift direction. In this work, we focus on the synergy effects of co-existing EIs and EEs on BAE stability, which are investigated numerically using the MAS code based on a Landau fluid–gyrokinetic hybrid model incorporating the kinetic effects of bulk plasma and energetic particle (EP) in a non-perturbative manner. It is found that for the center-peaked EI and EE pressure profiles that effectively drive i-BAE and e-BAE unstable, the synergy effects between EI and EE can lead to the stabilization for both i-BAE and e-BAE branches, which is attributed to the EP fluid convection and kinetic particle compression (KPC) responses that modify the magnetohydrodynamic (MHD) interchange and wave-particle resonances. The EP fluid convection response can enhance MHD interchange with center-peaked pressure profiles, which generally decreases the BAE frequency closer to ion acoustic wave and thus enhances the bulk plasma Landau damping. The passing EIs can resonate with both i-BAE and e-BAE through transit motion resonance, for which the KPC response provides drive for i-BAE with $\omega_p^*/\omega > 0$ and damping for e-BAE with $\omega_p^*/\omega < 0$ (where ω_p^* is the EI diamagnetic drift frequency). A stabilizing regime due to EE and EI synergy effects is then demonstrated for BAE, which is helpful for explaining experimental observations and control of Alfvén eigenmode activities through multiple auxiliary heating.

I. INTRODUCTION

In fusion experiments, energetic particles (EPs) can be produced through the processes of radio frequency (RF) wave heating and current drive, neutral beam injection (NBI), and fusion reactions, which are characterized by a much smaller population compared to the bulk plasma, while the pressure values are close to each other. The EP-related physics issues have received great attention in theory, simulation, and experiment over the past decades, which are strongly coupled to bulk plasmas and determine the overall plasma confinements.[1,2] Various shear Alfvén wave (SAW) instabilities in meso- and macro-scales can be destabilized by EPs through wave-particle resonance interactions and, in turn, lead to EP anomalous transports, including Alfvén eigenmodes (AEs), energetic particle modes (EPMs) and magnetohydrodynamic (MHD) modes. Specifically, the toroidal Alfvén eigenmode (TAE),[3,4] reversed shear Alfvén eigenmode (RSAE),[5] and beta-induced Alfvén eigenmode (BAE)[6,7] are considered the most important AEs responsible for EP redistribution and transport. This work aims to understand the synergy effects of energetic ion (EI) and energetic electron (EE) on BAE stability, for which the continuum accumulation point (CAP) is lifted due to the plasma geodesic compression, characterized by the geodesic acoustic mode (GAM) frequency but with a finite toroidal mode number $n > 0$.[8]

The BAE branches exist in both ion and electron diamagnetic drift directions with nearly symmetric frequency, which suffer continuum damping and radiative damping from bulk plasmas and are stable in the absence of EPs. As the power of RF/NBI heating and current drive increases, the EP drive eventually exceeds the threshold for over-bulk plasma damping, and the BAE becomes unstable and propagates in the EP diamagnetic drift direction. For example, the EI-driven BAE (i-BAE) is first identified in DIII-D experiment[9] with NBI and ion cyclotron resonance heating (ICRH) and later confirmed in many

other tokamaks, including TFTR,[10,11] FTU,[12,13] NSTX,[14] ASDEX-Upgrade,[15] Tore-Supra,[16] HL-2A,[17] KSTAR,[18] and J-TEXT.[19] The EE-driven BAEs are recently observed in HL-2A[20] and EAST tokamaks,[21–23] which utilize the electron cyclotron resonance heating (ECRH) and lower hybrid current drive (LHCD) that are favorable for EE generation. Both efforts in theory and simulation are performed to understand the linear properties of BAE. The theoretical framework of the general fishbone-like dispersion relation (GFLDR) demonstrates the (kinetic) BAE dispersion relation based on the gyrokinetic model.[6,24] Global gyrokinetic and kinetic-MHD hybrid simulations are successfully carried out to investigate EP excitation of BAE. Specifically, the i-BAEs are studied by XHMGC,[24–26] GTC,[27–31] ORB5,[32–34] and M3D-K,[35–37] and the e-BAEs are studied by GTC in analytic geometry[38] and HL-2A experimental geometry.[39]

Inspired by the observations on single e-BAE during ECRH[20] and single i-BAE during NBI heating[40] in HL-2A experiments, with applying more high-power heating approaches, abundant EEs and EIs can co-exist in the present-day experiments; however, their synergy effects on AE stability still remain to be understood. It should be pointed out that AE stabilities in the presence of multiple EIs have been numerically investigated, which are characterized by the positive charge sign with the same directions of diamagnetic drift and magnetic drifts. For instance, Fu *et al.* examined the impact of alpha particles and NBI-driven ions on TAE stability in TFTR,[41] while Varela *et al.* studied the influence of different NBI ion components on AEs in DIII-D.[42] Different from multiple EI species, the EE and EI have opposite charge signs, and their synergy effects on EI-driven TAE have been recently explored by MEGA simulation,[43] which is a relatively new topic in the community.

We investigate the synergy effects between EE and EI on BAE stability in this work using the global eigenvalue code MAS, which has been well benchmarked with gyrokinetic and kinetic MHD codes for AE[44–46] and MHD problems.[47] In MAS code, the bulk plasma is described by five-field Landau fluid model, which keeps the kinetic effects of electron/ion diamagnetic drifts and Landau damping, ion-finite Larmor radius (ion-FLR) and parallel electric fields beyond ideal MHD physics[44] and, thus, can faithfully capture the comprehensive bulk plasma damping for determining the excitation threshold of BAE, including continuum damping, radiative damping, and Landau damping. The drift-kinetic model is applied for describing EE dynamics, which separates the EE responses into adiabatic fluid convection and non-adiabatic kinetic particle compression (KPC) parts, which associates with the MHD interchange drive in reactive-type and wave-particle resonance drive in dissipative-type, respectively.[45] Both trapped and passing particles contribute to the EE adiabatic fluid convection response, while the EE KPC response is only contributed by trapped particles with the predominant precessional drift resonance, the transit motion resonance of passing EEs and the bounce-precession resonance of trapped EEs are ignored since corresponding characteristic frequencies are much higher than the BAE frequency. The gyrokinetic model is applied for describing EI physics; in addition to the precessional drift resonance of trapped EIs, it is further extended with EI orbital effects of FLR and finite orbit width (FOW) and transit motion resonance of passing EIs.[46] Based on the above numerical implementations, MAS code can capture both the bulk plasma damping and the EP drive effects in a non-perturbative manner, which facilitates the current study of BAE stability in the EI/EE parameter space.

In this paper, we choose two typical examples to demonstrate the synergy effects between EE and EI on the BAE dispersion relation and mode structure, specifically analyzing the passing EI effects on e-BAE and trapped EE effects on i-BAE, and the BAE growth rates exhibit a substantial decrease in both examples. Consequently, a stability window of BAE is found due to the mutual stabilization of i-BAE and e-BAE by EEs and EIs, which suggests a possible method for the active control of AE stability in experiments.

This paper is organized as follows: Sec. II presents the Landau fluid–gyrokinetic hybrid physical model of MAS code. Section III shows the simulation results of passing EI effects on e-BAE, trapped EE effects on i-BAE, and BAE stability window due to EE and EI synergy stabilization. Section IV gives the summary and discussion.

II. PHYSICAL MODEL

Beyond MHD physics, MAS code can be applied for the linear analyses of various plasma instabilities with crucial kinetic effects, based on the Landau-fluid model for bulk plasma, the gyrokinetic model for EI species, and the drift-kinetic model for EE species that have been developed and benchmarked in early works.[44–46] In this work, we first combine the above models and numerical implementations in a single framework by self-consistently incorporating the EI- and EE-related terms into the bulk plasma model equations, which read the vorticity equation:

$$\begin{aligned}&\left[\frac{\partial}{\partial t}\left(1+0.75\rho_i^2\nabla_\perp^2\right)+i\omega_{p,i}^*\right]\frac{c}{V_A^2}\nabla_\perp^2\delta\phi\\&+\mathbf{B}_0\cdot\nabla\left(\frac{1}{B_0}\nabla_\perp^2\delta A_\parallel\right)-\frac{4\pi}{c}\boldsymbol{\delta}\mathbf{B}\cdot\nabla\left(\frac{J_{\parallel 0}}{B_0}\right)\\&-8\pi(\nabla\delta P_i+\nabla\delta P_e)\cdot\frac{\mathbf{b}_0\times\boldsymbol{\kappa}}{B_0}\underbrace{-\sum_{h=ee,ei}\frac{4\pi Z_h}{c}\langle\mathbf{v}_\mathbf{d}\cdot\nabla\delta K_h\rangle_v}_{\{EP-KPC\}}\\&\underbrace{-\sum_{h=ee,ei}4\pi\nabla\left(\delta P_{\parallel h}^A+\delta P_{\perp h}^A\right)\cdot\frac{\mathbf{b}_0\times\boldsymbol{\kappa}}{B_0}}_{\{EP-IC\}}=0,\end{aligned}\tag{1}$$

the parallel Ohm's law:

$$\begin{aligned}\frac{\partial\delta A_\parallel}{\partial t}=&-c\mathbf{b}_0\cdot\nabla\delta\phi+\frac{cT_{e0}}{en_{e0}}\mathbf{b}_0\cdot\nabla\delta n_e+\frac{cT_{e0}}{en_{e0}B_0}\boldsymbol{\delta}\mathbf{B}\cdot\nabla n_{e0}\\&+\frac{cm_e}{e}\sqrt{\frac{\pi}{2}}\nu_{the}|k_\parallel|\delta u_{\parallel e}+\frac{c^2}{4\pi}\eta_\parallel\nabla_\perp^2\delta A_\parallel,\end{aligned}\tag{2}$$

the thermal ion pressure equation:

$$\begin{aligned}&\frac{\partial\delta P_i}{\partial t}+\frac{c\mathbf{b}_0\times\nabla\delta\phi}{B_0}\cdot\nabla P_{i0}+2\Gamma_{i\perp}P_{i0}c\nabla\delta\phi\cdot\frac{\mathbf{b}_0\times\boldsymbol{\kappa}}{B_0}\\&+\Gamma_{i\parallel}P_{i0}\mathbf{B}_0\cdot\nabla\left(\frac{\delta u_{\parallel i}}{B_0}\right)-i\Gamma_{i\perp}\omega_{p,i}^*Z_in_{i0}\rho_i^2\nabla_\perp^2\delta\phi\\&+2\Gamma_{i\perp}P_{i0}\frac{c}{Z_i}\nabla\delta T_i\cdot\frac{\mathbf{b}_0\times\boldsymbol{\kappa}}{B_0}+2\Gamma_{i\perp}T_{i0}\frac{c}{Z_i}\nabla\delta P_i\cdot\frac{\mathbf{b}_0\times\boldsymbol{\kappa}}{B_0}\\&+n_{i0}\frac{2}{\sqrt{\pi}}\sqrt{2}v_{thi}|k_\parallel|\delta T_i=0,\end{aligned}\tag{3}$$

the parallel momentum equation:

$$\frac{\partial \delta u_{\parallel i}}{\partial t} = -\frac{Z_i}{m_i}\frac{1}{en_{e0}}\left(\mathbf{b}_0\cdot\nabla\delta P_e + \frac{1}{B_0}\boldsymbol{\delta B}\cdot\nabla P_{e0}\right) - \frac{1}{m_i n_{i0}}\left(\mathbf{b}_0\cdot\nabla\delta P_i + \frac{1}{B_0}\boldsymbol{\delta B}\cdot\nabla P_{i0}\right) - \frac{Z_i}{m_i}\frac{m_e}{e}\sqrt{\frac{\pi}{2}}\nu_{the}|k_\parallel|\delta u_{\parallel e} - \frac{Z_i}{m_i}\frac{c}{4\pi}\eta_\parallel\nabla_\perp^2\delta A_\parallel, \quad (4)$$

and the ion continuity equation:

$$\frac{\partial \delta n_i}{\partial t} + \frac{c\mathbf{b}_0\times\nabla\delta\phi}{B_0}\cdot\nabla n_{i0} + 2cn_{i0}\nabla\delta\phi\cdot\frac{\mathbf{b}_0\times\boldsymbol{\kappa}}{B_0} + n_{i0}\mathbf{B}_0\cdot\nabla\left(\frac{\delta u_{\parallel i}}{B_0}\right) - i\omega_{p,i}^*\frac{Z_i n_{i0}}{T_{i0}}\rho_i^2\nabla_\perp^2\delta\phi + \frac{2c}{Z_i}\nabla\delta P_i\cdot\frac{\mathbf{b}_0\times\boldsymbol{\kappa}}{B_0} = 0, \quad (5)$$

where $\langle\cdots\rangle_v = \int \mathbf{dv} = \frac{2\pi B_0}{m_h}\int dv_\parallel d\mu$, $V_A = B_0/\sqrt{4\pi m_i n_{e0}}$ is the Alfvén speed calculated by using thermal ion mass and thermal electron density, $J_{\parallel 0} = \frac{c}{4\pi}\mathbf{b}_0\cdot\nabla\times\mathbf{B}_0$ is the parallel equilibrium current density, $\boldsymbol{\kappa} = \mathbf{b}_0\cdot\nabla\mathbf{b}_0$ is the magnetic field curvature, $\rho_i = v_{thi}/\Omega_{ci}$ is the ion Larmor radius, $v_{thi} = \sqrt{T_{i0}/m_i}$, $\Omega_{ci} = Z_iB_0/(cm_i)$, $\omega_{p,s}^* = \omega_{n,s}^* + \omega_{T,s}^*$ is the diamagnetic frequency ($\omega_{n,s}^* = -i\frac{cT_{s0}}{Z_sB_0}\mathbf{b}_0\times\frac{\nabla n_{s0}}{n_{s0}}\cdot\nabla$ and $\omega_{T,s}^* = -i\frac{c}{Z_sB_0}\mathbf{b}_0\times\nabla T_{s0}\cdot\nabla$), $\eta_\parallel = 0.51\frac{m_e\nu_{ei}}{n_{e0}e^2}$, and ν_{ei} is the electron–ion collision frequency. The subscript $s = i,e$ represents the ion and electron species of bulk plasmas. Equations (1)–(5) describe the dynamics of bulk plasmas and require closures of δP_e, δT_e, δT_i, δn_e, and $\delta u_{\parallel e}$ as follows:

$$\delta P_e = \delta n_e T_{e0} + n_{e0}\delta T_e, \quad (6)$$

$$\mathbf{b}_0\cdot\nabla\delta T_e + \frac{1}{B_0}\delta\mathbf{B}\cdot\nabla T_{e0} = 0, \quad (7)$$

$$\delta n_e = \frac{Z_i}{e}\delta n_i + \frac{c^2}{4\pi e V_A^2}\nabla_\perp^2\delta\phi + \underbrace{\sum_{h=ee,ei}\frac{Z_h}{e}\left(\delta n_h^A + \delta n_h^{NA}\right)}_{\{EP-density\}}, \quad (8)$$

$$en_{e0}\delta u_{\parallel e} = Z_i n_{i0}\delta u_{\parallel i} + \frac{c}{4\pi}\nabla_\perp^2\delta A_\parallel + \underbrace{\sum_{h=ee,ei} Z_h n_{h0}\delta u_{\parallel h}}_{\{EP-current\}}, \quad (9)$$

and

$$\delta T_i = \frac{1}{n_{i0}}(\delta P_i - \delta n_i T_{i0}). \quad (10)$$

The terms labeled by the brackets in Eqs. (1), (8), and (9) induce the EE and EI effects through the moments integrated from the perturbed distributions, which are separated into the adiabatic fluid and non-adiabatic kinetic parts as $\delta f_h = \delta f_h^A + \delta K_h$, with $h = ee, ei$ denoting EE and EI species. It should be pointed out that in Eq. (1), the EP-IC and EP-KPC terms refer to the EP-induced MHD interchange and kinetic compression effects, which arise from δf_h^A and δK_h, respectively. The adiabatic part δf_h^A describes the fluid property:[6,48]

$$\delta f_h^A = -\frac{Z_h}{T_{h0}}\Delta\phi J_0 f_{h0} - \frac{Z_h}{T_{h0}}\frac{\omega_{p,h}^*}{\omega}J_0\delta\psi f_{h0}, \quad (11)$$

where the first term indicates compression response to ion–acoustic fluctuations, the second term indicates convection response to shear-Alfvénic fluctuations being much larger than the first term for Alfvénic modes, and the adiabatic part δf_h^A is referred to as adiabatic fluid convection response in this work. $\Delta\phi = \delta\phi - \delta\psi$, $\omega_{p,h}^* = \omega_{n,h}^* + \omega_{T,h}^*\left(\frac{m_h v_\parallel^2 + 2\mu B_0}{2T_{h0}} - \frac{3}{2}\right)$, $\delta\psi$ is defined by $\partial\delta A_\parallel/\partial t = -c\mathbf{b_0}\cdot\nabla\delta\psi$, and $J_0 = J_0\left(\sqrt{b_h}v_\perp/v_{thh}\right)$ is the Bessel function for the FLR effects with $b_h = k_\perp^2\rho_h^2$, $\rho_h = v_{thh}/\Omega_{c,h}$ is the EP thermal cyclotron radius, and $v_{thh} = \sqrt{T_{h0}/m_h}$. In the drift-kinetic limit, the FLR effects can be ignored by setting $J_0 = 1$. The non-adiabatic part δK_h describes the kinetic particle compression response, for which the governing equation can be obtained from the gyrokinetic Vlasov equation for total δf_h[6,48] and Eq. (11) as

$$\left(\frac{v_\parallel}{\mathfrak{J}B_0}\partial_\theta + i\frac{nqv_\parallel}{\mathfrak{J}B_0} - i(\omega-\omega_d)\right)\delta K_h = -i\frac{Z_h}{T_{h0}}(\omega-\omega_{p,h}^*)\left(\Delta\phi + \frac{\omega_d}{\omega}\delta\psi\right)J_0 f_{h0}, \quad (12)$$

where $\omega_d = -i\mathbf{v_d}\cdot\nabla$, and $\mathfrak{J}$ is the Jacobian of Boozer coordinates (ψ,θ,ζ) defined by $\mathfrak{J}^{-1} = \nabla\psi\times\nabla\theta\cdot\nabla\zeta$. The δK_h solution of Eq. (12) differs between magnetically trapped and passing particles, which are obtained based on deeply trapped and well-circulating approximations, respectively.[45,46] To close the system of Eqs. (1)–(10), the EE and EI moments are calculated by integrating the perturbed distributions in velocity space. Specifically, the EP moments related to δf_h^A can be analytically derived for Maxwellian equilibrium as

$$\delta n_h^A = \int J_0\delta f_h^A\mathbf{dv} = -\frac{Z_h n_{h0}}{T_{h0}}\Delta\phi\Gamma_0 - \frac{Z_h n_{h0}}{T_{h0}}\frac{\omega_{n,h}^*}{\omega}\delta\psi\Gamma_0 - \frac{Z_h n_{h0}}{T_{h0}}\frac{\omega_{T,h}^*}{\omega}\delta\psi(-b_h\Gamma_0 + b_h\Gamma_1), \quad (13)$$

$$\delta u_{\parallel h}^A = \frac{1}{n_{h0}}\int v_\parallel J_0\delta f_h^A\mathbf{dv} = 0, \quad (14)$$

$$\delta P_{\parallel h}^A = \int m_h v_\parallel^2 J_0\delta f_h^A\mathbf{dv} = -Z_h n_{h0}\Delta\phi\Gamma_0 - Z_h n_{h0}\delta\psi\left\{\frac{\omega_{n,h}^*}{\omega} + \frac{\omega_{T,h}^*}{\omega}[(1-b_h)\Gamma_0 + b_h\Gamma_1]\right\}, \quad (15)$$

$$\delta P_{\perp h}^A = \int \mu B_0 J_0\delta f_h^A\mathbf{dv} = -Z_h n_{h0}\Delta\phi[(1-b_h)\Gamma_0 + b_h\Gamma_1] - Z_h n_{h0}\delta\psi\left\{\frac{\omega_{n,h}^*}{\omega}[(1-b_h)\Gamma_0 + b_h\Gamma_1] + \frac{\omega_{T,h}^*}{\omega}\left[(1-3b_h+2b_h^2)\Gamma_0 + (2b_h - 2b_h^2)\Gamma_1\right]\right\}, \quad (16)$$

where $\Gamma_0(b_h) = I_0(b_h)e^{-b_h}$, $\Gamma_1(b_h) = I_1(b_h)e^{-b_h}$, and I is the modified Bessel function of the first kind. To guarantee the accuracy of FOW effects in both long- and short-wavelength regimes, a velocity space integration algorithm is developed for numerical calculation of non-adiabatic EP moments:[46]

$$\delta n_h^{NA} = \int J_0\delta K_h\mathbf{dv}, \quad (17)$$

$$\delta u_{\parallel h}^{NA} = \frac{1}{n_{h0}}\int v_\parallel J_0\delta K_h\mathbf{dv}, \quad (18)$$

$$\delta P_{\parallel h}^{NA} = \int m_h v_\parallel^2 J_0 \delta K_h \mathbf{dv}, \tag{19}$$

$$\delta P_{\perp h}^{NA} = \int \mu B_0 J_0 \delta K_h \mathbf{dv}. \tag{20}$$

Note that the non-adiabatic pressures of Eqs. (19) and (20) are proportional to EP-KPC terms in Eq. (1). For Alfvénic modes with minor EP species, we only consider the EP effects from EP-IC and EP-KPC terms in Eq. (1), which are related to EP pressure moments in Eqs. (15), (16), (19), and (20) that dominate over density and parallel velocity perturbations.[45,46] In addition to numerical integrations of the above EP non-adiabatic moments with FOW effects, for the limiting case of zero-orbit-width (ZOW), Eqs. (17)–(20) can be derived analytically based on deeply trapped and well-circulating approximations, which are given in Appendix A. It is worthwhile mentioning that the deeply trapped and well-circulating approximations are adopted for EP species in MAS framework at the current stage,[45,46] which would be sufficient for describing the dynamics of most EP population in high-aspect ratio tokamaks. However, the barely trapped and barely circulating EEs generated during various RF-heated processes can resonantly interact with and destabilize fishbones[49] and TAEs,[50] which require a general treatment on orbit integrator and velocity space integration in full λ domain ($\lambda = \mu B_a/E$ denotes the pitch angle) and are beyond the scope of this study. Recently, the action angle approach has been successfully applied for calculating wave-particle resonances in full λ domain,[51,52] which can be adopted by the MAS model in future development. Regarding BAE excitations by different EP species, MAS has been verified with GTC gyrokinetic simulation for e-BAE in Ref. 45, and the i-BAE comparison between two codes is introduced in Appendix B.

III. SIMULATION RESULTS

In this section, we carry out MAS simulations to investigate the effects of EE/EI adiabatic fluid convection and non-adiabatic KPC responses on BAE stability, which couple to bulk plasma through the EP-IC and EP-KPC terms in Eq. (1), respectively. The adiabatic fluid convection response [Eq. (11)] already incorporates both the passing and trapped particle contributions, while the non-adiabatic KPC responses rely on the specific wave-particle resonance of each charge species. To delineate the underlying physics clearly, the EI and EE adiabatic fluid convection responses are fully kept with δf_{ei}^A and δf_{ee}^A, while the non-adiabatic KPC responses are calculated using the passing EI and trapped EE particles, based on the considerations of passing EI transit motion resonance and trapped EE precessional drift resonance, respectively, namely, $\delta K_{ei} \approx \delta K_{ei}^{passing}$ and $\delta K_{ee} \approx \delta K_{ee}^{trapped}$. In contrast, the transit motion frequency of passing EE is much larger than the BAE frequency, for which the non-adiabatic KPC response is almost zero with $\delta K_{ee}^{passing} \approx 0$. Despite additional orbit effects (FLR and FOW) and higher order precession-bounce resonance, the non-adiabatic KPC response of trapped EI is similar to that of trapped EE with precessional drift resonance, which becomes more important as EI temperature increases. After clarifying the EI effects on e-BAE stability and EE effects on i-BAE stability, we shall show the existence of a BAE stability window due to the synergy effects between EE and EI.

To isolate the influence of geometry complexity on BAE physics, a concentric circular geometry is applied in simulation, with the on-axis magnetic field strength $B_0 = 1.91$ T, the major radius $R_0 = 1.60$ m, and the minor radius $a = 0.29R_0$. The safety factor profile is given by $q = 1.3721 + 0.5\hat{\psi} - 0.1\hat{\psi}^2$, where $\hat{\psi} = \psi/\psi_w$ represents the normalized poloidal magnetic flux with ψ_w being the wall value. The radial profiles of safety factor q and magnetic shear $s = \frac{r}{q}\frac{dq}{dr}$ are shown in Fig. 1(a), where the $q = 1.5$ rational surface is located at $\rho_{tor} = 0.5$. The proton is applied for both thermal ion and EI species with $Z_i = Z_{ei} = e$ and $m_i = m_{ei} = m_p$. The bulk plasma temperatures and thermal electron density are uniform with $T_{e0} = 2$ keV, $T_{i0} = 0.5T_{e0}$, and $n_{e0} = 1.3 \times 10^{20}$ m^{-3}. The EP temperature T_h is also uniform and varies in different simulations. Both EE and EI utilized the density profile described by

$$n_{h0} = C_h n_{e0}\left\{1.0 + 0.24\left[\tanh\left(\left(0.26 - \hat{\psi}\right)/0.1\right) - 1.0\right]\right\}, \tag{21}$$

where the subscript $h = ei, ee$ stands for EI and EE species, and $C_h \sim [0, 1]$ is the control parameter for EP density. The radial profiles of normalized EP density $n_h/(C_h n_{e0})$ and density gradient intensity $|R_0/L_{n,h}|$ are shown in Fig. 1(b), which peaks at $q = 1.5$ rational surface with the maximum value of $|R_0/L_{n,h}| = 12$, and $L_{n,h} = (\nabla n_{h0}/n_{h0})^{-1}$ represents the EP density scale length. The thermal ion density n_{i0} is then determined by the quasi-neutrality condition $Z_i n_{i0} = e(n_{e0} + n_{ee}) - Z_{ei} n_{ei}$. In this work, we use 200 radial grid points and 2560 poloidal grid points and keep both the principal dominant m-harmonic and sidebands $m \in [nq - 1, nq + 1]$ for BAE simulations, which are enough for BAE physics in high-aspect ratio tokamak with the above parameters. The numerical convergence of our simulation results has been confirmed.

In the following, eight BAE cases are simulated with different EE and EI physics for $n = 4$ mode, which are described in Table I. It should be noted that the EE-IC/EI-IC (i.e., EP-IC) labeled by the bracket in Eq. (1) refer to the EP counterpart of the MHD interchange term, which associate with the EP adiabatic fluid convection response δf_h^A, and the EE-KPC/EI-KPC terms in Eq. (1) associate with the EP

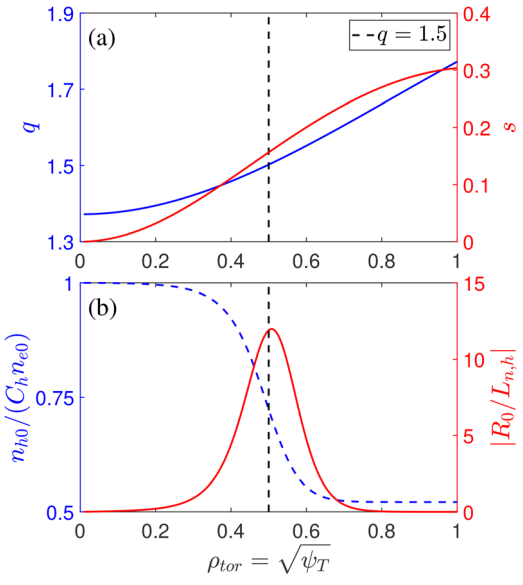

FIG. 1. (a) The radial profiles of safety factor q and magnetic shear $s = \frac{r}{q}\frac{dq}{dr}$. (b) The normalized EP density profile of $n_h/(C_h n_{e0})$ and EP density gradient intensity $|R_0/L_{n,h}|$, and $L_{n,h} = (\frac{1}{n_h}\frac{dn_h}{dr})^{-1}$.

TABLE I. Various simulation cases with different combinations of EI and EE physics. The EE and EI effects refer to the predominant EP-IC and EP-KPC terms labeled by the brackets in Eq. (1), which associate with δf_h^A and δK_h. Cases (I)–(IV) focus on the EI effects on e-BAE stability, and cases (V)–(VIII) focus on the EE effects on i-BAE stability.

Case	Branch	T_{ee}/T_{e0}	n_{ee}/n_{e0}	EE effects	T_{ei}/T_{e0}	n_{ei}/n_{e0}	EI effects
(I)	e-BAE	$\sim[5,30]$	$\sim[0,0.1]$	EE-IC trapped EE-KPC	None	None	None
(II)					9	0.02	EI-IC passing EI-KPC
(III)					9	0.03	
(IV)					9	0.02	EI-IC
(V)	i-BAE	None	None	None			
(VI)		17.5	0.04	EE-IC trapped EE-KPC	$\sim[5,25]$	$\sim[0,0.05]$	EI-IC passing EI-KPC
(VII)		17.5	0.06				
(VIII)		17.5	0.04	EE-IC			

non-adiabatic KPC response δK_h. Specifically, the e-BAEs propagating along electron diamagnetic drift direction are investigated in cases (I)–(IV), which are damped by bulk plasmas and excited unstable by trapped EEs in the parameter space of n_{ee} and T_{ee}. Different EI effects are induced to e-BAEs: no EI in case (I), $n_{ei}/n_{e0}=0.02$ and $T_{ei}/T_{e0}=9$ in case (II), $n_{ei}/n_{e0}=0.03$ and $T_{ei}/T_{e0}=9$, and a controlled simulation is conducted in case (IV) using the same n_{ei} and T_{ei} of case (II) but dropping the EI-KPC term in Eq. (1). Similarly, the i-BAEs propagating along the ion diamagnetic drift direction are investigated in cases (V)–(VIII), which are damped by bulk plasmas and excited unstable by the passing EIs in the parameter space of n_{ei} and T_{ei}. Different EE effects are induced to i-BAEs: no EE in case (V), $n_{ee}/n_{e0}=0.04$ and $T_{ee}/T_{e0}=17.5$ in case (VI), $n_{ee}/n_{e0}=0.06$ and $T_{ee}/T_{e0}=17.5$ in case (VII), and a controlled simulation is conducted in case (VIII) using the same n_{ee} and T_{ee} of case (VI) but dropping EE-KPC term in Eq. (1).

A. EI effects on e-BAE stability

We first analyze the e-BAE dispersion relation with different EI effects in cases (I)–(IV), to clarify the roles of opposite charge species EI on e-BAE stability. In these cases, the dominant EE-IC and trapped EE-KPC terms in Eq. (1) are kept, and the e-BAE can be excited through the precessional drift resonance with trapped EEs. Meanwhile, comprehensive bulk plasma damping effects are kept in the MAS model,[44] including continuum damping, radiative damping, and Landau damping by both thermal ions and thermal electrons. The e-BAE stability can then be determined by the competition between the EE drive and bulk plasma damping, for which the real frequency ω_r and growth rate γ dependencies on EE density n_{ee} and EE temperature T_{ee} are shown in Figs. 2(a) and 2(e). It is seen that $|\omega_r|$ decreases as n_{ee} and T_{ee} increase; the reason is that δf_{ee}^A with center-peaked pressure profile, the MHD interchange effect is enhanced through the EE-IC term in Eq. (1), which non-perturbatively decreases the absolute value of e-BAE real frequency.[45] The γ value of e-BAE exhibits non-monotonic variations with both n_{ee} and T_{ee}, resulting in an island-like unstable spectrum. In the regime of $\beta_{ee}\ll\beta_{e0}$, the EE drive cannot overcome bulk plasma damping, and the e-BAE is stable with $\gamma<0$. In the regime of $\beta_{ee}\sim\beta_{e0}$, the drop of $|\omega_r|$, due to EE-IC, is small, while the trapped EE-KPC drive quickly increases either through n_{ee} for EE population or through T_{ee} for the resonance condition, the e-BAE γ value increases to the maximal amplitude. In the regime of $\beta_{ee}\gg\beta_{e0}$, the frequency mismatch breaks the resonance condition between trapped EE and e-BAE, due to the large decrease in $|\omega_r|$ by EE-IC or the large increase in trapped EE precession frequency, which weakens the trapped EE-KPC drive and enhances the bulk plasma damping.

The EI effects are induced in cases (II)–(IV), by choosing EI temperature of $T_{ei}/T_{ee}=9$ to satisfy the transit motion resonance between the passing EIs and e-BAE, and keeping the same EE physics as in case (I). As EI density n_{ei} gradually increases in cases (I)–(III), the overall e-BAE $|\omega_r|$ decreases slightly by comparing Figs. 2(a)–2(c), attributing to the small enhancement of MHD interchange effect by perturbative EIs with center-peaked pressure profile. The e-BAE γ is sensitive to EI fraction, and the unstable domain size exhibits an obvious reduction when comparing Figs. 2(e)–2(g). For example, cases (I)–(III) give the minimal critical value of EE-β for e-BAE excitation as $\min(\beta_{ee,crit})=0.91\%,1.85\%,2.28\%$, which show increase trend that implies the e-BAE damping enhancement by EIs. To understand the underlying mechanism of EI stabilization, a controlled simulation is conducted in case (IV) using the same n_{ei} and T_{ei} parameters with case (II), and case (IV) differs from case (II) by only keeping the EI-IC term while removing the passing EI-KPC term in Eq. (1). Comparing the results of cases (I), (II), and (IV) in Fig. 2, we conclude that the EI-IC term in Eq. (1) is mainly responsible for the slight decrease in e-BAE $|\omega_r|$, while the passing EI-KPC term in Eq. (1) is mainly responsible for the large decrease in e-BAE γ. Specifically, two EI stabilization routes for e-BAE can be identified in the regime of $\beta_{ei}\ll\beta_{e0}$. The first route is the transit motion resonance with e-BAE that leads to the direct damping through the passing EI-KPC term, which is intuitive from the theoretical expression of δP_{ei}^{NA}. Considering the ideal MHD approximation of $\delta\phi=\delta\psi$ and the uniform T_{ei}, Eq. (A5) reduces to

$$\delta P_{ei}^{NA}\approx -4Z_{ei}n_{ei}\frac{\omega_{D,ei}}{\omega}\delta\psi\left(1-\frac{\omega_{n,ei}^*}{\omega}\right)F_{FLR}, \tag{22}$$

based on the Maxwellian EI equilibrium distribution. In the bracket of Eq. (22), the first term "1" comes from the negative energy derivative of $\frac{\partial f_{ei}}{\partial E}<0$, which represents the EI Landau damping. The second term is related to the radial derivative $\frac{\partial f_{ei}}{\partial r}$ and mode frequency, which can either drive or damp modes relying on the sign. For center-peaked EI pressure profile with positive $\omega_{n,ei}^*>0$ and e-BAE propagating along the electron diamagnetic drift direction with negative $\omega<0$, the sign of the second term $-\omega_{n,ei}^*/\omega>0$ is consistent with the first term "1"; thus, the spatial gradient of passing EI distribution with center-peaked pressure profile can stabilize the e-BAE. This mechanism is consistent

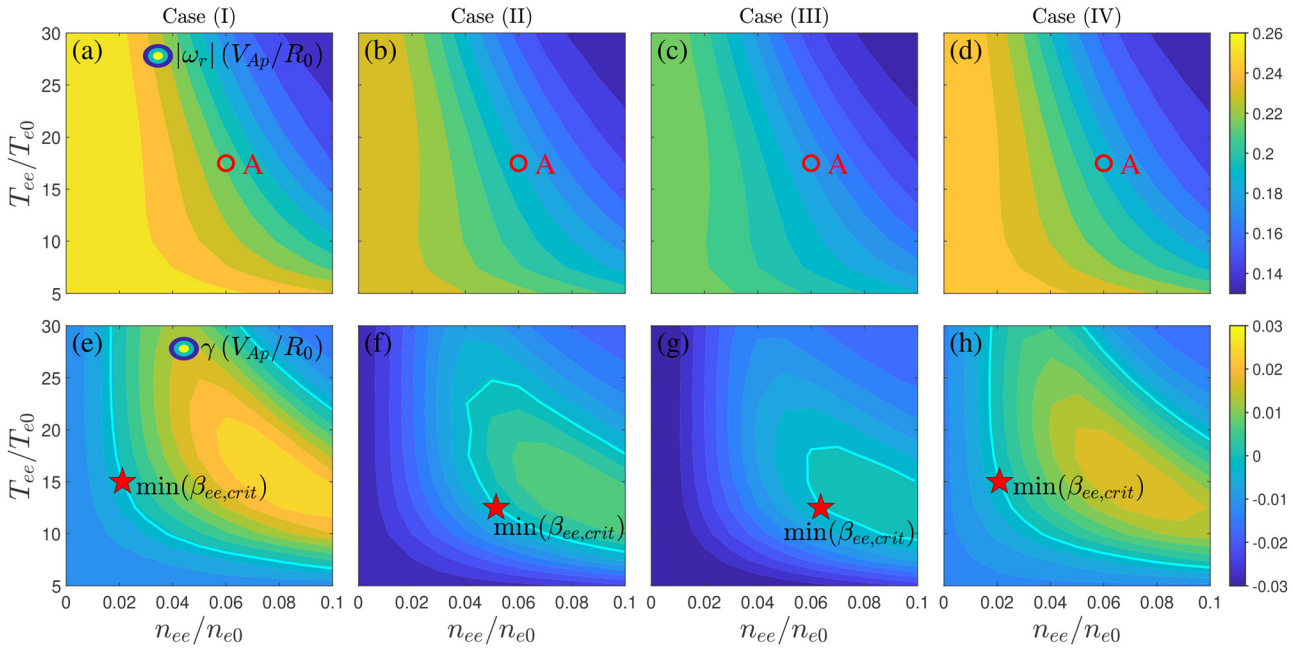

FIG. 2. MAS simulations of $n = 4$ e-BAE dispersion relation with different EI effects in cases (I)–(IV). The first and second rows show the dependencies of e-BAE real frequency ω_r and growth rate γ on EE density n_{ee} and temperature T_{ee}. The cyan solid lines represent the e-BAE stability boundary with $\gamma = 0$, and the red pentagrams represent the locations of n_{ee} and T_{ee} parameters corresponding to the minimal value of critical EE-β for e-BAE excitation, i.e., $\min(\beta_{ee,crit}) = 0.91\%, 1.85\%, 2.28\%, 0.90\%$ for cases (I)–(IV).

with the theoretical framework of EP-AE interaction reviewed by Ref. 53. The second route is the non-perturbative EI effect that decreases e-BAE $|\omega_r|$ through the EI-IC term, which leads to the reduction of the frequency gap between e-BAE and ion acoustic wave and thus enhances the bulk plasma Landau damping. In the regime of $\beta_{ei} \ll \beta_{e0}$ adopted by cases (II)–(IV) simulations, the first route plays the dominant role on EI stabilization of e-BAE, while the second route is sub-dominant due to the smallness of EI-β that is perturbative to e-BAE fluctuations. Figure 3 shows the e-BAE mode structure of the electrostatic potential $\delta\phi$ in cases (I)–(IV), which are barely modified by EIs with $\beta_{ei} \ll \beta_{e0}$ in consistent with the slight decrease in e-BAE $|\omega_r|$. In a short summary, the EIs with center-peaked pressure profile can effectively stabilize e-BAE in the perturbative regime of $\beta_{ei} \ll \beta_{e0}$ when EI diamagnetic drift frequency is opposite to the e-BAE frequency in sign $\omega^*_{n,ei}/\omega < 0$, which primarily attributes to the dissipative damping induced by passing EIs through transit motion resonance.

B. EE effects on i-BAE stability

We further analyze the i-BAE properties in cases (V)–(VIII) using the same geometry and bulk plasma parameters, in which the EI and EE species switch roles compared to e-BAE cases. Specifically, the passing EIs are responsible for the i-BAE excitation through transit motion resonance, while EEs are added as the opposite charge species that modify i-BAE stability. Case (V) corresponds to the EI-driven i-BAE without additional EEs, for which the real frequency ω_r and growth rate γ dependencies on EI density n_{ei} and temperature T_{ei} are shown in Figs. 4(a) and 4(e), respectively. In the regime of $\beta_{ei} \leq \beta_{e0}$ that is common in experiments, the i-BAE ω_r is barely changed by EIs, while the i-BAE γ can quickly increase with increasing the EI drive intensity, which overcomes the bulk plasma damping and becomes unstable. The EE effects are induced in cases (VI)–(VIII), including the EE adiabatic fluid convection response δf^A_{ee} for EE-IC term and trapped EE non-adiabatic KPC response $\delta K^{trapped}_{ee}$ for EE-KPC term in Eq. (1). Though the precessional drift frequency amplitude of trapped EEs is on the same order as i-BAE frequency, the trapped EEs cannot interact with i-BAEs through wave-particle resonance due to the opposite motion direction, for which the response to i-BAE fluctuations is reactive-type. It should be pointed out that barely trapped EE with a small population has the ion-direction precession drift, which is not considered in the MAS model that treats the trapped particle dynamics based on deeply trapped approximation in the leading order. Different from the efficient stabilization of e-BAE by the passing EI resonance damping, EE cannot alter i-BAE stability in the perturbative regime of $\beta_{ee} \ll \beta_{e0}$ due to the lack of resonance condition; thus, the relatively large n_{ee} and T_{ee} are chosen for EEs to satisfy the non-perturbative condition of $\beta_{ee} \sim \beta_{e0}$, which indirectly affects the i-BAE through non-perturbative modifications on the real frequency and mode structure.

As shown in Figs. 4(a)–4(c), the i-BAE real frequency ω_r decreases up to $\sim$30% by gradually increasing the EE fraction in cases (V)–(VII). Consequently, the bulk plasma damping is enhanced due to the frequency downshift, and the i-BAE growth rates significantly decrease as indicated by Figs. 4(e)–4(g). In case (VIII), we use the same n_{ee} and T_{ee} parameters as in case (VI), while keeping the EE-IC term and removing the trapped EE-KPC term in Eq. (1), and carry out a

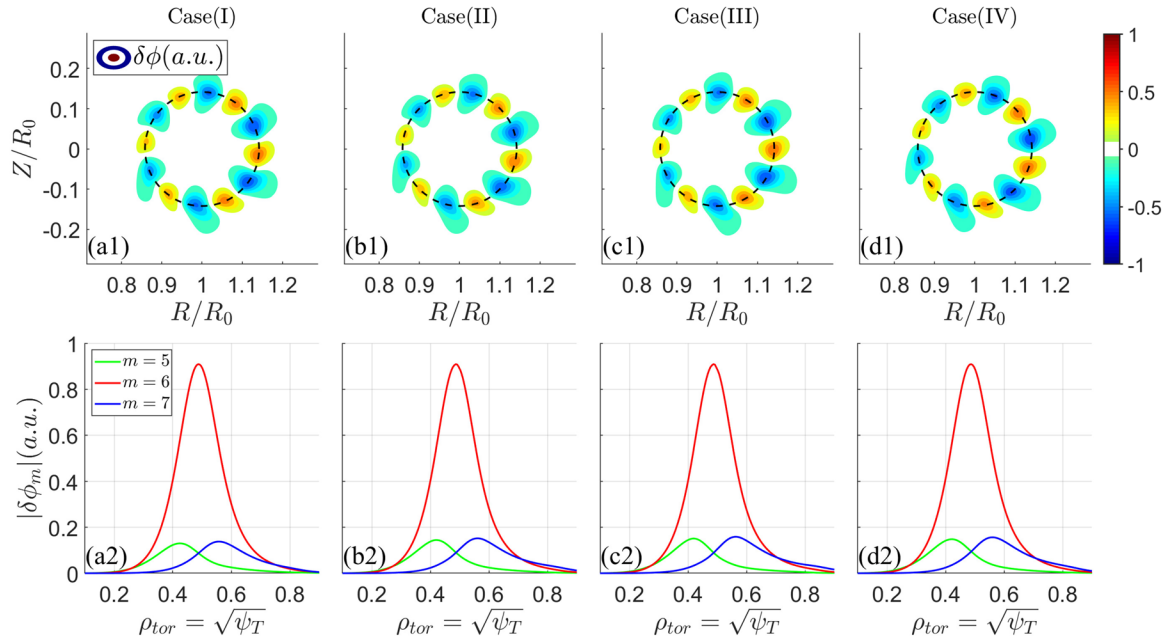

FIG. 3. The $n = 4$ e-BAE 2D poloidal mode structures of electrostatic potential $\delta\phi$ in cases (I)–(IV) (first row) and the corresponding 1D radial profiles of each m-harmonics (second row), which correspond to the A points in Figs. 2(a)–2(d).

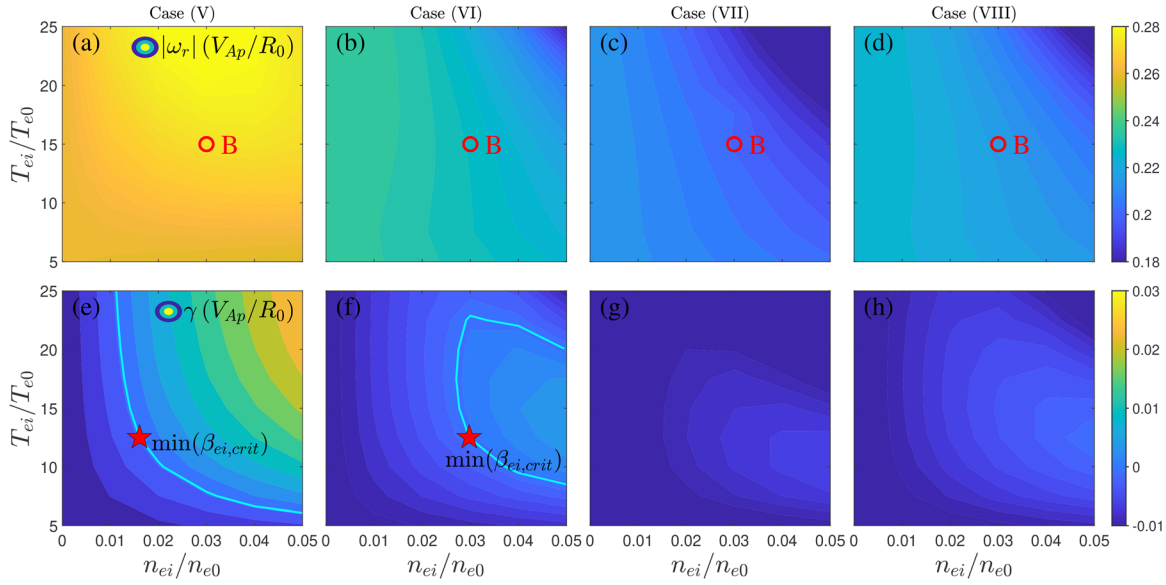

FIG. 4. MAS simulations of $n = 4$ i-BAE dispersion relation with different EE effects in cases (V)–(VIII). The first and second rows show the dependencies of i-BAE real frequency ω_r and growth rate γ on EI density n_{ei} and temperature T_{ei}. The cyan solid lines represent the i-BAE stability boundary with $\gamma = 0$, and the red pentagrams represent the locations of n_{ei} and T_{ei} parameters corresponding to the minimal value of critical EI-β for i-BAE excitation, i.e., $\min(\beta_{ei,crit}) = 0.58\%, 1.07\%, \infty, \infty$ for cases (V)–(VIII).

controlled simulation to clarify the role of trapped EE-KPC term on i-BAE stability. From cases (V), (VI), and (VIII) in Fig. 4, it is seen that both the i-BAE ω_r and γ show larger reductions in case (VIII) compared to case (VI), which indicates that the EE-IC term for MHD interchange enhancement is weakened by the trapped EE-KPC term. The reason can be understood by comparing $\delta P^A_{\parallel,\perp ee}$ and δP^{NA}_{ee}, which are proportional to EE-IC and trapped EE-KPC terms in Eq. (1), respectively. Considering the uniform T_{ee} profile and zero Larmor radius (ZLR) for EEs, and the ideal MHD approximation of $\delta\phi = \delta\psi$, Eqs. (15) and (16) reduce to

$$\delta P^{A}_{\parallel ee} = \delta P^{A}_{\perp ee} \approx -q_e n_{ee} \frac{\omega^{*}_{n,ee}}{\omega} \delta\psi, \tag{23}$$

and Eq. (A10) reduces to

$$\delta P^{NA}_{ee} \approx f_t q_e n_{ee} \frac{\omega^{*}_{n,ee}}{\omega} R_5\left(\sqrt{\zeta}\right) \delta\psi, \tag{24}$$

where f_t is the trapped EE fraction, R_5 is the trapped EE response function, $\zeta = \omega/\omega_{D,ee}$, and $\omega_{D,ee} = -i\frac{cT_{ee}}{q_e}\frac{\mathbf{b_0}\times\boldsymbol{\kappa}}{B_0}\cdot\nabla|_{\theta=0}$ reflects the EE precession frequency after integration average over the Maxwellian distribution. As shown in Fig. 5, in the regime of $\zeta = \omega/\omega_{D,ee} < 0$ for a negative ratio between i-BAE frequency and EE precession frequency, the imaginary parts of R_5 and δP^{NA}_{ee} are zero [i.e., $\mathrm{Im}(R_5) = 0$ and $\mathrm{Im}(\delta P^{NA}_{ee}) = 0$ without wave-particle resonance], the positive real part of $\mathrm{Re}(R_5) > 0$ leads to the opposite sign between δP^{NA}_{ee} and δP^{A}_{ee} that cancels each other out up to the trapped particle fraction f_t, which results in a near-zero trapped EE net response to ion direction modes. This physics picture is consistent with the observation in gyrokinetic simulations of ion temperature gradient (ITG) mode with trapped thermal electrons,[54] and both demonstrate the destabilization of ion direction modes by trapped electrons. Figure 6 shows the i-BAE mode structure of electrostatic potential $\delta\phi$ in cases (V)–(VIII). In case (V) without EEs, it is seen from Fig. 6(a2) that the dominant $m = 6$ poloidal harmonic amplitude is much larger that the $m = 5$ and $m = 7$ sidebands, which correspond to a weakly ballooning structure in Fig. 6(a1). After adding non-perturbative EEs with $\beta_{ee} \sim \beta_{e0}$ in cases (VI)–(VIII), the $m = 5$ and $m = 7$ sideband harmonic amplitudes drastically increase as shown in Figs. 6(b2)–6(d2), which exhibit more typical ballooning characters in Figs. 6(b1)–6(d1) due to the enhanced MHD interchange effect by EEs. In a short summary, the EEs can only stabilize i-BAEs indirectly, for which fluid response leads to the i-BAE frequency downshift that suffers more bulk plasma damping, and this stabilization route becomes important in the non-perturbative regime of $\beta_{ee} \sim \beta_{e0}$.

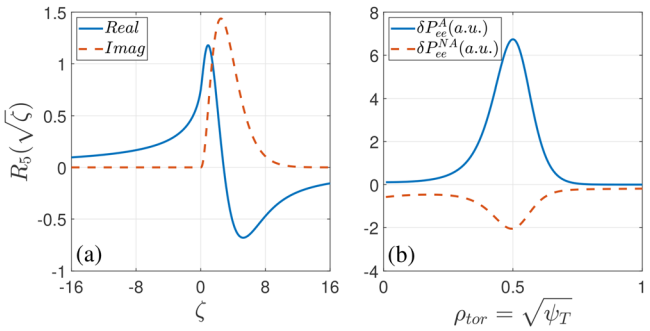

FIG. 5. (a) The real and imaginary parts of EE response function $R_5(\sqrt{\zeta})$. (b) The radial profiles of EE adiabatic pressure δP^{A}_{ee} in Eq. (23) and trapped EE non-adiabatic pressure δP^{NA}_{ee} in Eq. (24) using the parameters of B point in Fig. 4(b) of case (VI).

C. BAE stability window due to synergy effects between EE and EI

As discussed above, the EIs can stabilize e-BAE but destabilize i-BAE, and the EEs can stabilize i-BAE but destabilize e-BAE, which are complementary and both play dual roles. To intuitively understand the EE and EI synergy effects on the overall BAE stability, we compare the solutions using single and double EP species for both i-BAE and e-BAE branches. For the double EP species simulation, the EE parameters are fixed as $n_{ee}/n_{e0} = 0.06$ and $T_{ee}/T_{e0} = 17.5$, which can effectively drive e-BAE and damp i-BAE in the non-perturbative regime of $\beta_{ee} \sim \beta_{e0}$. Two groups of simulations are conducted using EI temperature $T_{ei}/T_{e0} = 9$ and $T_{ei}/T_{e0} = 25$, which correspond to strong and weak passing EI transit motion resonances. The EI density n_{ei}/n_{e0} is varied for β_{ei} (i.e., EI-β) scan. For a single EP species simulation, we keep the EP species for mode excitation while removing the opposite charge species, and other conditions are the same as the double EP species simulation.

Compared to the single EP species results, the double EP species results of $|\omega_r|$ exhibit modest reductions for both i-BAE and e-BAE branches in Figs. 7(a) and 7(b), and the reductions become larger with increasing β_{ei}, which is due to the MHD interchange enhancement by the EE-IC and EI-IC terms. Importantly, the i-BAE and e-BAE are simultaneously stabilized by EE and EI synergy effects, for which the growth rates are smaller than the single EP species results in Figs. 7(c)

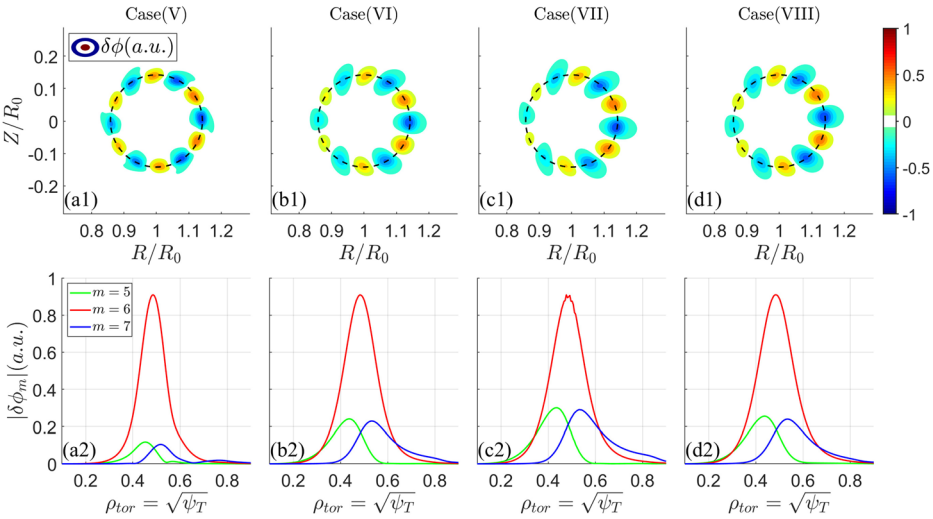

FIG. 6. The $n = 4$ i-BAE 2D poloidal mode structures of electrostatic potential $\delta\phi$ in cases (V)–(VIII) (first row) and the corresponding 1D radial profiles of each m-harmonics (second row), which correspond to the B points in Figs. 4(a)–4(d).

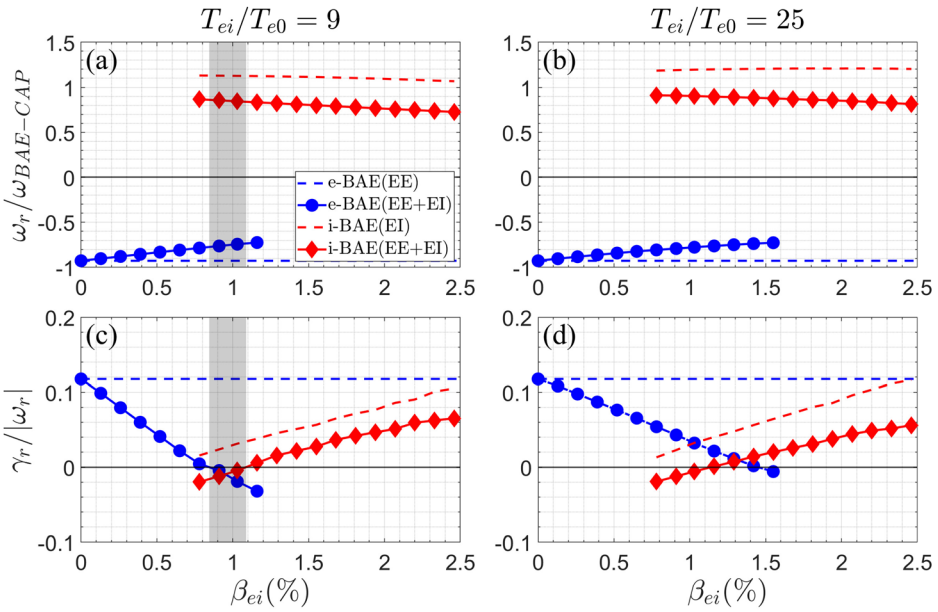

FIG. 7. The $n = 4$ i-BAE/e-BAE dispersion relations with different EI parameters, and the EE parameters are fixed with $n_{ee}/n_{e0} = 0.06$ and $T_{ee}/T_{e0} = 17.5$. The solid marker lines represent the cases with EI and EE synergy effects, while the dashed lines represent the cases with only EP species for excitation. $\omega_{BAE-CAP}$ represents the frequency of BAE continuum accumulation point.

and 7(d). For fixed EE parameters in our simulation, the BAE stability window appears with proper EI parameters of $\beta_{ei} \sim 1\%$ and $T_{ei}/T_{e0} = 9$, which can effectively stabilize e-BAE before the i-BAE destabilization, as indicated by the gray-shaded region in Fig. 7(c). In Fig. 7(d), the passing EI transit motion resonance becomes weaker for $T_{ei}/T_{e0} = 25$, and the e-BAE growth rate curve decreases to zero at a higher β_{ei} value compared to $T_{ei}/T_{e0} = 9$; however, the i-BAE growth rate curve remains close to $T_{ei}/T_{e0} = 9$ due to the stronger trapped EI precessional drift resonance at $T_{ei}/T_{e0} = 25$ (note that trapped EIs are newly added in this subsection).

IV. SUMMARY AND DISCUSSION

Motivated by the observations of e-BAE and i-BAE activities in RF-heated plasma,[20,40] we analyze the synergy effects of EE and EI on BAE stability in this work. The global eigenvalue code MAS is applied for the BAE dispersion relation and mode structure calculations in an analytic equilibrium, which adopts a Landau fluid–gyrokinetic hybrid physics model with necessary kinetic effects that treat bulk plasma damping and EP drive on an equal footing and thus enables the existence of excitation threshold in the parameter space of EP density and temperature. The effects of both adiabatic fluid convection and non-adiabatic KPC response of multiple EP species on BAE unstable spectra are investigated in detail, and the main conclusions are summarized as follows:

(i) For the e-BAE driven by trapped EEs through precessional drift resonance that propagates along electron diamagnetic drift direction, the passing EIs have stabilization effects on e-BAE through indirect and direct processes: the EIs with center-peaked pressure profile can enhance the MHD interchange from the adiabatic fluid convection response, which then non-perturbatively decrease the absolute value of e-BAE frequency to be more closer to ion acoustic wave frequency and thus weaken the BAE growth rate indirectly by enhancing the bulk plasma Landau damping. Meanwhile, the passing EIs can interact with e-BAE through transit motion resonance; however, EI diamagnetic drift frequency is opposite to e-BAE frequency in sign, which leads to the direct damping in dissipative-type related to the non-adiabatic KPC response.

(ii) For the i-BAE driven by passing EIs through transit motion resonance that propagates along the ion diamagnetic drift direction, there is no resonance condition to be satisfied with the trapped EEs, which is characterized by the precession drift along the electron diamagnetic drift direction. Therefore, the trapped EEs only stabilize i-BAE through the indirect process, namely, the EE adiabatic fluid convection response leads to the decrease in i-BAE frequency so that the mode growth rate is weakened by the enhanced bulk plasma Landau damping. However, for i-BAE fluctuations, the non-adiabatic KPC response of trapped EEs is dominated by the real part in reactive-type rather than the imaginary part due to wave-particle resonance, which partially cancels the adiabatic fluid convection response and results in the near-zero net response of trapped EEs. Thus, the i-BAE is mainly stabilized by the adiabatic fluid convection response of the passing EEs.

(iii) In the presence of EEs and EIs, both i-BAE and e-BAE can be excited; however, their growth rates are smaller than in single EP species cases without synergy effects. For a particular BAE branch propagating along either ion or electron diamagnetic drift direction, a stabilizing regime can be achieved by inducing a suitable amount of EPs with opposite charge, which weakens the counter-propagation BAE fluctuations while the drive is still below the threshold for co-propagation BAE excitation.

For reactor parameter regions such as ITER, where the EP temperature is significantly higher, the direct damping from EIs on the e-BAE may become weak due to the mismatch of resonance condition. However, the indirect damping mechanisms are expected to remain

operative. Therefore, the synergistic stabilization from oppositely charged EPs is anticipated to persist, which is beneficial for plasma confinement. These findings are helpful for understanding the experimental observations and providing possible methods for AE activity control. However, our current study utilizes the center-peaked pressure profiles for both EE and EI species, and the results might change qualitatively for the off-axis peaked EP profiles, which will be the focus of our future study.

ACKNOWLEDGMENTS

This work is supported by the National Natural Science Foundation of China under Grant Nos. 12025508, 12275351, and 11905290 and the Strategic Priority Research Program of the Chinese Academy of Sciences under Grant Nos. XDB0500302 and XDB0790202.

AUTHOR DECLARATIONS

Conflict of Interest

The authors have no conflicts to disclose.

Author Contributions

L. Z. Guo: Conceptualization (equal); Formal analysis (lead); Methodology (equal); Validation (equal); Writing – original draft (equal); Writing – review & editing (equal). **J. Bao:** Conceptualization (equal); Methodology (equal); Validation (equal); Writing – review & editing (equal). **W. L. Zhang:** Conceptualization (equal); Methodology (equal); Validation (equal); Writing – review & editing (equal). **Z. Lin:** Methodology (supporting); Writing – review & editing (supporting).

DATA AVAILABILITY

The data that support the findings of this study are available from the corresponding authors upon reasonable request.

APPENDIX A: ANALYTIC EXPRESSIONS OF NON-ADIABATIC EP MOMENTS IN ZERO ORBIT WIDTH LIMIT

If we omit the FOW effect and consider well-circulating EIs, the non-adiabatic distribution δK_{ei} is presented by

$$\delta K_{ei} = \frac{1}{\omega - k_\parallel v_\parallel}\left[\frac{Z_h}{T_{h0}}\omega\Delta\phi J_0 f_{h0} - \frac{Z_h}{T_{h0}}\omega^*_{p,h}\Delta\phi J_0 f_{h0} - i\frac{Z_h}{T_{h0}}\mathbf{v_d}\cdot\nabla\delta\psi J_0 f_{h0} + i\frac{Z_h}{T_{h0}}\frac{\omega^*_{p,h}}{\omega}\mathbf{v_d}\cdot\nabla\delta\psi J_0 f_{h0}\right]. \tag{A1}$$

The deeply trapped EE non-adiabatic distribution δK_{ee} can be written as

$$\delta K_{ee} = \frac{\omega}{\omega - \bar{\omega}_d}\frac{Z_h}{T_{h0}}\left(1 - \frac{\omega^*_{p,h}}{\omega}\right)(\bar{\delta\phi} - \bar{\delta\psi})f_{h0} + \frac{1}{\omega - \bar{\omega}_d}\frac{Z_h}{T_{h0}}\left(1 - \frac{\omega^*_{p,h}}{\omega}\right)\omega_d\bar{\delta\psi}f_{h0}, \tag{A2}$$

where $\bar{\omega}_d = \oint\omega_d(dl/v_\parallel)/\tau_b$ is the precession frequency, $\tau_b = \oint(dl/v_\parallel)$ is the bounce period, and l is the traveled distance of the trapped particle along the magnetic field line in one bounce motion period.

With $\int\mathbf{dv} = \frac{2\pi B_0}{m_h}\int dv_\parallel d\mu = 2\pi v_\perp\int dv_\parallel dv_\perp$, integrating Eq. (A2) in velocity space, we can derive EI non-adiabatic moments as

$$\delta n_h^{NA} = -\frac{Z_h n_{h0}}{T_{h0}}\Delta\phi D_{FLR} - 2\frac{Z_h n_{h0}}{T_{h0}}\frac{\omega_D}{\omega}N_{FLR}, \tag{A3}$$

$$\delta u_{\parallel h} = -2\frac{Z_h}{T_{h0}}\frac{\omega}{k_\parallel}\Delta\phi\left[C_1\left(1 - \frac{\omega^*_{n,h}}{\omega} + (C_1 - C_3)\frac{\omega^*_{T,h}}{\omega}\right)\right] - \frac{Z_h}{T_{h0}}\frac{\omega}{k_\parallel}\Delta\phi D_{FLR} - 2\frac{Z_h}{T_{h0}}\frac{\omega_D}{\omega}\frac{\omega}{k_\parallel}\delta\psi(C_1 + C_3) \times\left(1 - \frac{\omega^*_{n,h}}{\omega} - \frac{\omega^*_{T,h}}{\omega}\right) - 2\frac{Z_h}{T_{h0}}\frac{\omega_D}{\omega}\frac{\omega}{k_\parallel}\delta\psi N_{FLR}, \tag{A4}$$

$$\delta P_h^{NA} = \delta P_{\parallel h}^{NA} + \delta P_{\perp h}^{NA} = -2Z_h n_{h0}\Delta\phi N_{FLR} - 4Z_h n_{h0}\frac{\omega_D}{\omega}\delta\psi \times\left[\left(1 - \frac{\omega^*_{n,h}}{\omega}\right)F_{FLR} - \frac{\omega^*_{T,h}}{\omega}G_{FLR}\right], \tag{A5}$$

where $\omega_D = -i\frac{cT_{h0}}{Z_h}\frac{\mathbf{b}_0\times\boldsymbol{\kappa}}{B_0}\cdot\nabla$. The response function D_{FLR}, N_{FLR}, F_{FLR}, and G_{FLR} are

$$\begin{aligned}
D_{FLR} &= 2\left(1 - \frac{\omega^*_{n,h}}{\omega}\right)C_1\zeta_h Z(\zeta_h) - 2\frac{\omega^*_{T,h}}{\omega}\left[C_1\left(\zeta_h^3 Z(\zeta_h) - \frac{3}{2}\zeta_h Z(\zeta_h) + \zeta_h^2\right) + C_3\zeta_h Z(\zeta_h)\right],\\
N_{FLR} &= 2\left(1 - \frac{\omega^*_{n,h}}{\omega}\right)\left[C_1\left(\zeta_h^3 Z(\zeta_h) + \zeta_h^2\right) + \frac{1}{2}C_3\zeta_h Z(\zeta_h)\right]\\
&\quad -2\frac{\omega^*_{T,h}}{\omega}\left[C_1\left(\zeta_h^5 Z(\zeta_h) + \zeta_h^4 + \frac{1}{2}\zeta_h^2\right) + \frac{3}{2}(C_3 - C_1)\left(\zeta_h^3 Z(\zeta_h) + \zeta_h^2\right) + \left(\frac{1}{2}C_5 - \frac{3}{4}C_3\right)\zeta_h Z(\zeta_h)\right],\\
F_{FLR} &= 2C_1\left[\zeta_h^5 Z(\zeta_h) + \zeta_h^4 + \frac{1}{2}\zeta_h^2\right] + 2C_3\left[\zeta_h^3 Z(\zeta_h) + \zeta_h^2\right] + \frac{1}{2}C_5\zeta_h Z(\zeta_h),\\
G_{FLR} &= \frac{1}{2}C_7\zeta_h Z(\zeta_h) + C_5\left[\frac{5}{2}\zeta_h^3 Z(\zeta_h) - \frac{3}{4}\zeta_h Z(\zeta_h) + \frac{5}{2}\zeta_h^2\right] + C_3\left[4\zeta_h^5 Z(\zeta_h) + 4\zeta_h^4 - 3\zeta_h^3 Z(\zeta_h) - \zeta_h^2\right]\\
&\quad + C_1\left[2\zeta_h^7 Z(\zeta_h) + 2\zeta_h^6 - 3\zeta_h^5 Z(\zeta_h) - 2\zeta_h^4\right],
\end{aligned} \tag{A6}$$

where $Z(\zeta_h)$ is the plasma dispersion function: $Z(\zeta_h) = \frac{1}{\sqrt{\pi}}\int_{-\infty}^{+\infty}\frac{\exp(-t^2)}{t-\zeta_h}dt$ and $\zeta_h = \omega/\left(\sqrt{2}k_\parallel v_{thh}\right)$. The subscript "FLR" means the modifications of EI response functions D, N, F, and G when we reserve the FLR effect. If we ignore the FLR effect, these response functions would reduce to the same form as that in Ref. 6, except for an extra ζ_h factor. The coefficient C_n used in the response functions is given by $C_n(b_h) = \int_0^\infty \hat{v}_\perp^n J_0^2\left(\sqrt{2b_h}\hat{v}_\perp\right)e^{-\hat{v}_\perp^2}d\hat{v}_\perp$, where $\hat{v}_\perp = v_\perp/\left(\sqrt{2}v_{thh}\right)$. The specific expressions of C_1, C_3, C_5, C_7 are as follows:

$$\begin{aligned} C_1 &= \frac{1}{2}e^{-b_h}I_0(b_h),\\ C_3 &= \frac{1}{2}e^{-b_h}[(1-b_h)I_0(b_h)+b_hI_1(b_h)],\\ C_5 &= \frac{1}{2}e^{-b_h}\left[2(1-b_h)^2I_0(b_h)+b_h(3-2b_h)I_1(b_h)\right],\\ C_7 &= \frac{1}{2}e^{-b_h}\left[(6-18b_h+17b_h^2-4b_h^3)I_0(b_h)\right.\\ &\quad\left.+b_h(11-15b_h+4b_h^2)I_1(b_h)\right], \end{aligned} \tag{A7}$$

where $b_h = k_\perp^2\rho_h^2$, and $\rho_h = v_{thh}/\Omega_{c,h}$ is the EI thermal cyclotron radius. Using the same method, the EE non-adiabatic moments can be obtained as

$$\begin{aligned} \delta n_h^{NA} &= -f_t\frac{Z_hn_{h0}}{T_{h0}}\left[2\left(1-\frac{\omega_{n,h}^*}{\omega}+\frac{3}{2}\frac{\omega_{T,h}^*}{\omega}\right)\zeta R_1\left(\sqrt{\zeta}\right)-2\frac{\omega_{T,h}^*}{\omega}\zeta R_3\right.\\ &\quad\left.\times\left(\sqrt{\zeta}\right)\right]\Delta\phi - f_t\frac{Z_hn_{h0}}{T_{h0}}\left[2\left(1-\frac{\omega_{n,h}^*}{\omega}+\frac{3}{2}\frac{\omega_{T,h}^*}{\omega}\right)\right.\\ &\quad\left.\times R_3\left(\sqrt{\zeta}\right)-2\frac{\omega_{T,h}^*}{\omega}R_5\left(\sqrt{\zeta}\right)\right]\delta\psi, \end{aligned} \tag{A8}$$

$$\begin{aligned} \delta u_{\parallel h}^{NA} &= -\frac{Z_h}{T_{h0}}\frac{\omega}{k_\parallel}(1-f_t)\left(1-\frac{\omega_{n,h}^*}{\omega}\right)\Delta\phi-2\frac{Z_h}{T_{h0}}\frac{\omega}{k_\parallel}\\ &\quad\times\left(\frac{\omega_{D,h}}{\omega}-f_t\frac{3}{4}\frac{\omega_{D0,h}}{\omega}\right)\left(1-\frac{\omega_{n,h}^*}{\omega}-\frac{\omega_{T,h}^*}{\omega}\right)\delta\psi, \end{aligned} \tag{A9}$$

$$\begin{aligned} \delta P_h^{NA} &= -f_tZ_hn_{h0}\left[\left(1-\frac{\omega_{n,h}^*}{\omega}+\frac{3}{2}\frac{\omega_{T,h}^*}{\omega}\right)\zeta R_3\left(\sqrt{\zeta}\right)-\frac{\omega_{T,h}^*}{\omega}\zeta R_5\right.\\ &\quad\left.\times\left(\sqrt{\zeta}\right)\right]\Delta\phi - f_tZ_hn_{h0}\left[\left(1-\frac{\omega_{n,h}^*}{\omega}+\frac{3}{2}\frac{\omega_{T,h}^*}{\omega}\right)\right.\\ &\quad\left.\times R_5\left(\sqrt{\zeta}\right)-\frac{\omega_{T,h}^*}{\omega}R_7\left(\sqrt{\zeta}\right)\right]\delta\psi, \end{aligned} \tag{A10}$$

where $\omega_{D0,h} = -i\frac{cT_{h0}}{Z_h}\frac{\mathbf{b}_0\times\boldsymbol{\kappa}}{B_0}\cdot\nabla|_{\theta=0}$, $f_t = \sqrt{1-\lambda_{low}\frac{B_0}{B_a}}$ is the trapped particle fraction for the Maxwellian equilibrium distribution, $B_a/B_{max} < \lambda_{low} < B_a/B_0$ is the lower cutoff trapped pitch angle, $\zeta = \omega/\omega_{D0,h}$, and the EE response functions are given by

$$\begin{aligned} R_1\left(\sqrt{\zeta}\right) &= 1+\sqrt{\zeta}Z\left(\sqrt{\zeta}\right),\\ R_3\left(\sqrt{\zeta}\right) &= \frac{1}{2}+\zeta+(\zeta)^{3/2}Z\left(\sqrt{\zeta}\right),\\ R_5\left(\sqrt{\zeta}\right) &= \frac{3}{4}+\frac{1}{2}\zeta+\zeta^2+(\zeta)^{5/2}Z\left(\sqrt{\zeta}\right),\\ R_7\left(\sqrt{\zeta}\right) &= \frac{15}{8}+\frac{3}{4}\zeta+\frac{1}{2}\zeta^2+\zeta^3+(\zeta)^{7/2}Z\left(\sqrt{\zeta}\right). \end{aligned} \tag{A11}$$

APPENDIX B: COMPARISON OF I-BAE BETWEEN MAS AND GTC SIMULATIONS

We carry out MAS and GTC simulations of i-BAE in analytic geometry based on a well-established benchmark case.[27,28] The thermal electron, thermal ion, and EI temperatures are uniform with $T_{i0} = T_{e0} = 500$ eV and $T_{ei} = 25T_{e0}$, and the thermal electron density is uniform with $n_{e0} = 1.3\times10^{14}$ cm^{-3}. The EI density profile is described by $n_{ei}/n_{ei,a} = 1.0 + 0.27[\tanh((0.26-\hat{\psi})/0.06) - 1.0]$ (where $n_{ei,a}$ is the on-axis value, and $\hat{\psi} = \psi/\psi_w$ is the normalized poloidal flux), and the reciprocal of EI density scale length $|R_0/L_{n,ei}| = 20$ peaks at $q = 2$ rational surface. The on-axis magnetic field strength is $B_0 = 1.91$ T, the major radius is $R_0 = 1.0$ m, and the minor radius is $a = 0.333R_0$. The safety factor profile is $q = 1.797 + 0.8\hat{\psi} - 0.2\hat{\psi}^2$.

As shown in Fig. 8, both the real frequency ω and growth rate γ increase with increasing EI fraction n_{ei}/n_{e0} from MAS and GTC simulations. The ω obtained from the two codes show excellent agreement. The γ results show relatively large difference, which may originate from two aspects: (i) MAS applies a Landau-fluid model for the thermal ion species, which results in different bulk plasma damping from GTC gyrokinetic model; and (ii) MAS adopts the well-circulating and deeply trapped approximations for EI species, which might weaken/strengthen the EI drive in phase space depending on specific resonance condition.

The $\delta\phi$ mode structure of i-BAE is compared between GTC and MAS simulations in Fig. 9. Different from e-BAE reported in Ref. 45 that MAS and GTC give very similar mode structure, the i-BAE mode structure exhibit differences in the poloidal shape and radial width; this is due to the fact that deeply trapped EEs are the dominant drive for e-BAE so that the deeply trapped approximated model in MAS can well describe the EE response, while the i-BAE can resonantly interact with EIs in much wider phase space domains as shown in the appendix of Ref. 45, which amplifies the

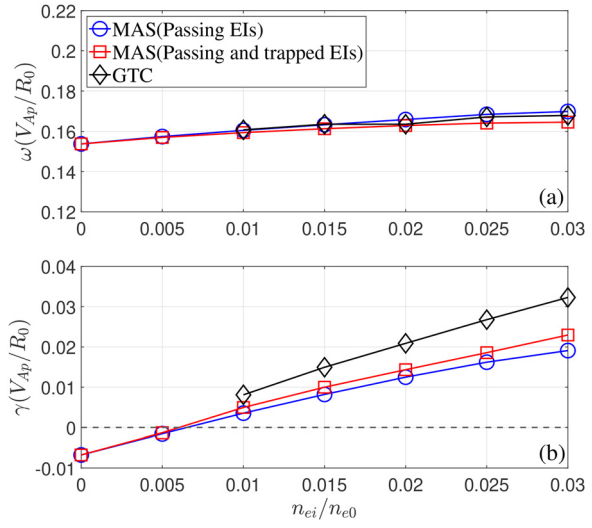

FIG. 8. The comparisons of $n = 3$ i-BAE (a) real frequency ω and (b) growth rate γ between MAS (blue and red colors) and GTC (black color) simulations. The EI temperature is fixed as $T_{ei} = 25T_{e0}$.

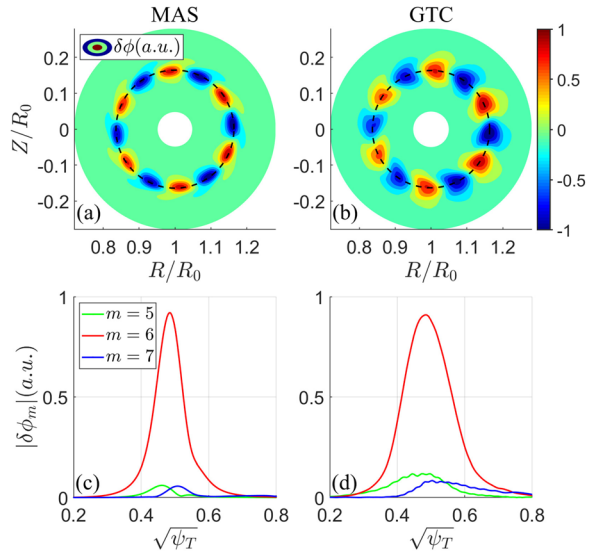

FIG. 9. The comparisons of $n = 3$ i-BAE 2D poloidal mode structures of electrostatic potential $\delta\phi$ in MAS (left panel) and GTC (right panel) simulations. Here the EI temperature is $T_{ei} = 25T_{e0}$ and the EI density is $n_{ei} = 0.01n_{e0}$.

difference between GTC exact model and MAS well-circulating/deeply trapped approximated model, in consistent with the growth rate difference in Fig. 8(b). For the qualitative investigation of i-BAE excitation and damping in the current work, the MAS model can faithfully capture the leading physics of i-BAE following the GFLDR theory.[6]

REFERENCES

[1]S. Pinches, H. Berk, D. Borba, B. Breizman, S. Briguglio, A. Fasoli, G. Fogaccia, M. Gryaznevich, V. Kiptily, M. Mantsinen *et al.*, "The role of energetic particles in fusion plasmas," Plasma Phys. Controlled Fusion **46**, B187 (2004).

[2]A. Fasoli, C. Gormenzano, H. Berk, B. Breizman, S. Briguglio, D. Darrow, N. Gorelenkov, W. Heidbrink, A. Jaun, S. Konovalov *et al.*, "Physics of energetic ions," Nucl. Fusion **47**, S264 (2007).

[3]C. Cheng and M. Chance, "Low-n shear alfvén spectra in axisymmetric toroidal plasmas," Phys. Fluids **29**, 3695–3701 (1986).

[4]L. Chen and F. Zonca, "Theory of shear Alfvén waves in toroidal plasmas," Phys. Scr. **60**, 81 (1995).

[5]H. Berk, D. Borba, B. Breizman, S. Pinches, and S. Sharapov, "Theoretical interpretation of Alfvén cascades in tokamaks with nonmonotonic Q profiles," Phys. Rev. Lett. **87**, 185002 (2001).

[6]F. Zonca, L. Chen, and R. A. Santoro, "Kinetic theory of low-frequency Alfvén modes in tokamaks," Plasma Phys. Controlled Fusion **38**, 2011 (1996).

[7]W. Heidbrink, E. Ruskov, E. Carolipio, J. Fang, M. Van Zeeland, and R. James, "What is the "beta-induced Alfvén eigenmode?"," Phys. Plasmas **6**, 1147–1161 (1999).

[8]M. Chu, J. Greene, L. Lao, A. Turnbull, and M. Chance, "A numerical study of the high-n shear Alfvén spectrum gap and the high-n gap mode," Phys. Fluids B: Plasma Phys. **4**, 3713–3721 (1992).

[9]W. Heidbrink, E. Strait, M. Chu, and A. Turnbull, "Observation of beta-induced Alfvén eigenmodes in the diii-d tokamak," Phys. Rev. Lett. **71**, 855 (1993).

[10]R. Nazikian, Z. Chang, E. Fredrickson, E. Mazzucato, S. Batha, R. Bell, R. Budny, C. Bush, C. Cheng, A. Janos *et al.*, "High-frequency core localized modes in neutral beam heated plasmas on TFTR," Phys. Plasmas **3**, 593–605 (1996).

[11]W. Heidbrink, S. H. Batha, R. Bell, Z. Chang, D. Darrow, J. Fang, E. Fredrickson, R. James, F. Levington, R. Nazikian *et al.*, "Search for alpha driven baes in TFTR," Nucl. Fusion **36**, 1725 (1996).

[12]P. Buratti, P. Smeulders, F. Zonca, S. Annibaldi, M. D. Benedetti, H. Kroegler, G. Regnoli, O. Tudisco, and the FTU-Team, "Observation of high-frequency waves during strong tearing mode activity in FTU plasmas without fast ions," Nucl. Fusion **45**, 1446 (2005).

[13]S. V. Annibaldi, F. Zonca, and P. Buratti, "Excitation of beta-induced Alfvén eigenmodes in the presence of a magnetic island," Plasma Phys. Controlled Fusion **49**, 475 (2007).

[14]D. Darrow, E. Fredrickson, N. Gorelenkov, A. Roquemore, and K. Shinohara, "MHD induced neutral beam ion loss from NSTX plasmas," Nucl. Fusion **48**, 084004 (2008).

[15]P. Lauber, M. Br dgam, D. Curran, V. Igochine, K. Sassenberg, S. Günter, M. Maraschek, M. García-Muñoz, N. Hicks, and the ASDEX Upgrade Team, "Kinetic Alfvén eigenmodes at ASDEX upgrade," Plasma Phys. Controlled Fusion **51**, 124009 (2009).

[16]C. Nguyen, X. Garbet, R. Sabot, L. Eriksson, M. Goniche, P. Maget, V. Basiuk, J. Decker, D. Elbeze, G. Huysmans *et al.*, "Excitation of beta Alfvén eigenmodes in tore-supra," Plasma Phys. Controlled Fusion **51**, 095002 (2009).

[17]HL-2A Team, "Investigation of beta-induced Alfvén eigenmode during strong tearing mode activity in the HL-2A tokamak," J. Phys. Soc. Jpn. **79**, 044501 (2010).

[18]M. J. Hole, C. M. Ryu, M. H. Woo, J. G. Bak, S. E. Sharapov, M. Fitzgerald, and the KSTAR Team, "First evidence of Alfvén wave activity in KSTAR plasmas," Plasma Phys. Controlled Fusion **55**, 045004 (2013).

[19]L. Liu, J. He, Q. Hu, and G. Zhuang, "Observation of beta-induced Alfvén eigenmode in J-TEXT tokamak," Plasma Phys. Controlled Fusion **57**, 065007 (2015).

[20]W. Chen, X. Ding, Q. Yang, Y. Liu, X. Ji, Y. Zhang, J. Zhou, G. Yuan, H. Sun, W. Li *et al.*, "β-induced Alfvén eigenmodes destabilized by energetic electrons in a tokamak plasma," Phys. Rev. Lett. **105**, 185004 (2010).

[21]M. Xu, W. Chen, L. Hu, R. Zhou, G. Zhong, T. Shi, L. Xu, Y. Zhang, Y. Sun, S. Lin *et al.*, "Experimental observation of beta-induced Alfvén eigenmodes during strong tearing modes on the east tokamak in fast-electron plasmas," Plasma Phys. Controlled Fusion **55**, 065002 (2013).

[22]N. Zhao, J. Bao, W. Chen, T. Shi, Z. Wang, N. Yan, S. Liu, H. Liu, Q. Zang, S. Lin *et al.*, "Multiple Alfvén eigenmodes induced by energetic electrons and nonlinear mode couplings in east radio-frequency heated h-mode plasmas," Nucl. Fusion **61**, 046013 (2021).

[23]Y. Chao, L. Xu, C. Mai, M. Wu, Y. Duan, S. Lin, K. Geng, C. Zhou, and L. Hu, "β-induced Alfvén eigenmodes and fishbone driven by energetic electrons in east electron heating dominant plasmas," Nucl. Fusion **64**, 036015 (2024).

[24]X. Wang, F. Zonca, and L. Chen, "Theory and simulation of discrete kinetic beta induced Alfvén eigenmode in tokamak plasmas," Plasma Phys. Controlled Fusion **52**, 115005 (2010).

[25]X. Wang, S. Briguglio, L. Chen, C. Di Troia, G. Fogaccia, G. Vlad, and F. Zonca, "An extended hybrid magnetohydrodynamics gyrokinetic model for numerical simulation of shear Alfvén waves in burning plasmas," Phys. Plasmas **18**, 052504 (2011).

[26]X. Wang, S. Briguglio, L. Chen, C. Di Troia, G. Fogaccia, G. Vlad, and F. Zonca, "Nonlinear dynamics of beta-induced Alfvén eigenmode driven by energetic particles," Phys. Rev. E **86**, 045401 (2012).

[27]H. Zhang, Z. Lin, I. Holod, X. Wang, Y. Xiao, and W. Zhang, "Gyrokinetic particle simulation of beta-induced Alfvén eigenmode," Phys. Plasmas **17**, 112505 (2010).

[28]H. Zhang, Z. Lin, and I. Holod, "Nonlinear frequency oscillation of Alfvén eigenmodes in fusion plasmas," Phys. Rev. Lett. **109**, 025001 (2012).

[29]H. Zhang, Z. Lin, W. Deng, I. Holod, Z. Wang, Y. Xiao, and W. Zhang, "Nonlinear dynamics of beta-induced Alfvén eigenmode in tokamak," Phys. Plasmas **20**, 012510 (2013).

[30]H. Zhang and Z. Lin, "Nonlinear generation of zonal fields by the beta-induced Alfvén eigenmode in tokamak," Plasma Sci. Technol. **15**, 969 (2013).

[31]Y. Liu, Z. Lin, H. Zhang, and W. Zhang, "Excitation of low frequency Alfvén eigenmodes in toroidal plasmas," Nucl. Fusion **57**, 114001 (2017).

[32]A. Biancalani, A. Bottino, P. Lauber, A. Mishchenko, and F. Vannini, "Effect of the electron redistribution on the nonlinear saturation of Alfvén eigenmodes and the excitation of zonal flows," J. Plasma Phys. **86**, 825860301 (2020).

[33]A. Biancalani, A. Bottino, A. Di Siena, Ö. Gürcan, T. Hayward-Schneider, F. Jenko, P. Lauber, A. Mishchenko, P. Morel, I. Novikau *et al.*, "Gyrokinetic investigation of Alfvén instabilities in the presence of turbulence," Plasma Phys. Controlled Fusion **63**, 065009 (2021).
[34]A. Biancalani, A. Bottino, D. Del Sarto, M. Falessi, T. Hayward-Schneider, P. Lauber, A. Mishchenko, B. Rettino, J. Sama, F. Vannini *et al.*, "Nonlinear interaction of Alfvénic instabilities and turbulence via the modification of the equilibrium profiles," J. Plasma Phys. **89**, 905890602 (2023).
[35]S. Duan, G. Fu, H. Cai, and D. Li, "Hybrid simulations of beta-induced Alfvén eigenmode with reversed safety factor profile," Nucl. Fusion **62**, 056002 (2022).
[36]S. Duan, X. Wang, H. Cai, and D. Li, "Simulations of nonlinear interaction between beta-induced Alfvén eigenmode and tearing mode," Nucl. Fusion **63**, 046002 (2023).
[37]S. Duan, X. Zhu, and H. Cai, "Simulations of beta-induced Alfvén eigenmode mitigation by off-axis energetic particle distribution," Nucl. Fusion **64**, 076002 (2024).
[38]J. Cheng, W. Zhang, Z. Lin, I. Holod, D. Li, Y. Chen, and J. Cao, "Gyrokinetic particle simulation of fast-electron driven beta-induced Aflvén eigenmode," Phys. Plasmas **23**, 052504 (2016).
[39]Y. Chen, W. Zhang, J. Cheng, Z. Lin, C. Dong, and D. Li, "Verification of an energetic-electron-driven β-induced Alfvén eigenmode in the HL-2A tokamak," Phys. Plasmas **26**, 102507 (2019).
[40]W. Chen, L. Yu, P. Shi, Y. Hou, Z. Shi, J. Bao, Z. Qiu, X. Ji, X. He, Y. Li *et al.*, "Nonlinear dynamics and effects of fast-ion driven instabilities in HL-2A NBI heating high-β n h-mode plasmas," Phys. Lett. **A 527**, 129983 (2024).
[41]G. Fu, C. Cheng, R. Budny, Z. Chang, D. Darrow, E. Fredrickson, E. Mazzucato, R. Nazikian, and S. Zweben, "Stability analysis of toroidicity-induced Alfvén eigenmodes in TFTR deuterium-tritium experiments," Phys. Rev. Lett. **75**, 2336 (1995).
[42]J. Varela, D. A. Spong, L. Garcia, Y. Todo, J. Huang, and M. Murakami, "Study of Alfven eigenmodes stability in plasma with multiple NBI driven energetic particle species," Phys. Plasmas **26**, 062502 (2019).
[43]J. Wang, Y. Todo, H. Wang, Z.-X. Wang, and M. Idouakass, "Stabilization of energetic-ion driven toroidal Alfvén eigenmode by energetic electrons in tokamak plasmas," Nucl. Fusion **60**, 106004 (2020).
[44]J. Bao, W. Zhang, D. Li, Z. Lin, G. Dong, C. Liu, H. Xie, G. Meng, J. Cheng, C. Dong *et al.*, "MAS: A versatile Landau-fluid eigenvalue code for plasma stability analysis in general geometry," Nucl. Fusion **63**, 076021 (2023).
[45]J. Bao, W. Zhang, D. Li, Z. Lin, Z. Qiu, W. Chen, X. Zhu, J. Cheng, C. Dong, and J. Cao, "Global simulations of kinetic-magnetohydrodynamic processes with energetic electrons in tokamak plasmas," Nucl. Fusion **64**, 016004 (2024).
[46]X. Xu, L. Guo, W. Sun, J. Bao, C. Dong, J. Cao, Z. Qiu, H. Cai, P. Liu, W. Zhang *et al.*, "Gyrokinetic modeling of energetic ion response to arbitrary-wavelength electromagnetic fluctuations in magnetized plasmas," Plasma Phys. Controlled Fusion **67**, 045032 (2025).
[47]G. Brochard, J. Bao, C. Liu, N. Gorelenkov, G. Choi, G. Dong, P. Liu, J. M. Clenaghan, J. Nicolau, F. Wang *et al.*, "Verification and validation of linear gyrokinetic and kinetic-MHD simulations for internal kink instability in DIII-D tokamak," Nucl. Fusion **62**, 036021 (2022).
[48]L. Chen and A. Hasegawa, "Kinetic theory of geomagnetic pulsations: 1. Internal excitations by energetic particles," J. Geophys. Res. Space Phys. **96**, 1503–1512, https://doi.org/10.1029/90JA02346 (1991).
[49]F. Zonca, P. Buratti, A. Cardinali, L. Chen, J.-Q. Dong, Y.-X. Long, A. Milovanov, F. Romanelli, P. Smeulders, L. Wang *et al.*, "Electron fishbones: Theory and experimental evidence," Nucl. Fusion **47**, 1588 (2007).
[50]T. Wang, X. Zhu, L. Zeng, S. Briguglio, G. Vlad, F. Zonca, and Z. Qiu, "Excitation of toroidal Alfvén eigenmode by barely circulating energetic electrons in low density plasmas," Plasma Phys. Controlled Fusion **65**, 055026 (2023).
[51]G. Wei, M. V. Falessi, T. Wang, F. Zonca, and Z. Qiu, "Calculation of toroidal ALFV n eigenmode mode structure in general axisymmetric toroidal geometry," Phys. Plasmas **31**, 072505 (2024).
[52]G. Wei, F. Zonca, M. V. Falessi, and Z. Qiu, "Excitation of toroidal Alfvén eigenmode by energetic particles in DTT and effect of negative triangularity," Nucl. Fusion **65**, 106035 (2025).
[53]Y. Todo, "Introduction to the interaction between energetic particles and Alfvén eigenmodes in toroidal plasmas," Rev. Mod. Plasma Phys. **3**(1), 1 (2019).
[54]Z. Lin, Y. Nishimura, Y. Xiao, I. Holod, W. Zhang, and L. Chen, "Global gyrokinetic particle simulations with kinetic electrons," Plasma Phys. Controlled Fusion **49**, B163 (2007).